Thermo-viscoplastic constitutive relation for aluminium alloys, modeling of negative strain rate sensitivity and viscous drag effects

Alexis Rusinek [a,*], J.A. Rodríguez-Martínez [b]

[a] National Engineering School of Metz (ENIM), Laboratory of Mechanics, Biomechanics, Polymers and Structures (LaBPS), Ile du Saulcy, 57000 Metz, France
[b] Department of Continuum Mechanics and Structural Analysis, University Carlos III of Madrid, Avda. de la Universidad 30, 28911 Leganés, Madrid, Spain

ABSTRACT

In this paper are presented two extensions of the Rusinek–Klepaczko constitutive relation [Rusinek A, Klepaczko JR. Shear testing of sheet steel at wide range of strain rates and a constitutive relation with strain-rate and temperature dependence of the flow stress. Int J Plasticity 2001;17:87–115] to define the behaviour of aluminium alloys at wide ranges of strain rate and temperature. The formulations reported extend the validity of the Rusinek–Klepaczko model for the definition of particular aspects of the behaviour of aluminium alloys, namely the negative strain rate sensitivity and the viscous drag. Such formulations are applied to describe the thermo-viscoplastic behaviour of two commercial aluminium alloys (*AA 5083-H116* and *AA 7075*) using experimental data available in the literature [Clausen AH, Børvik T, Hopperstad OS, Benallal A. Flow and fracture characteristics of aluminium alloy AA5083-H116 as function of strain rate, temperature and triaxiality. Mater Sci Eng A 2004;364:260–72; El-Magd E, Abouridouane M. Characterization, modelling and simulation of deformation and fracture behaviour of the light-weight wrought alloys under high strain rate loading. Int J Impact Eng 2006;32:741–58]. Their analytical results are compared with those obtained from the phenomenological constitutive relations reported in Clausen et al. (2004) and El-Magd and Abouridouane (2006). The best agreement with experiments is achieved by the predictions provided by the extended Rusinek–Klepaczko models. Moreover, the formulations presented may be implemented into **FE** code using for example the algorithm reported in [Zaera R, Fernández-Sáez J. An implicit consistent algorithm for the integration of thermoviscoplastic constitutive equations in adiabatic conditions and finite deformations. Int J Solids Struct 2006;43:1594–612].

© 2009 Elsevier Ltd. All rights reserved.

1. Introduction

Aluminium alloys (**AA**) gather an increasing interest in several engineering fields because of their notorious mechanical properties. Certain types of **AA** exhibit flow stress level comparable to that showed by steel alloys traditionally used in industrial applications [1]. In comparison with steel alloys, **AA** allow for considerable reduction in the weight of the structure. Nowadays **AA** find their use in many different applications such as marine constructions, train and ship components, aeronautical and crash-box structures Fig. 1a [2] and different types of lightweight protection systems.

Dynamic behaviour of **AA** has particular relevance in aeronautical industry. Aircraft-components, like fuselage or wings, are usually subjected to impact tests to guarantee their structural integrity under potential crash or accident, Fig. 1b [3]. During such loading condition the material is subjected to wide ranges of strain rate from quasi-static to high strain rates up to $\dot{\bar{\varepsilon}} \approx 10^4 \, \text{s}^{-1}$ [4], Fig. 2.

In that range of stain rates some **AA** exhibit two particular effects that strongly influence their thermo-viscoplastic behaviour. Those phenomena are negative strain rate sensitivity and viscous drag.

2. Theoretical considerations

Due to their complexity, the previous effects are rarely introduced in modeling of **AA** [1]. Inhibition of these phenomena in many steel alloys has induced the major developments in constitutive modeling conducted for steel in comparison with **AA**.

2.1. The negative strain rate sensitivity showed by certain AA under particular loading conditions

Some **AA** exhibit macroscopic negative strain rate sensitivity (**NSRS**), Eq. 1, from quasi-static to intermediate strain rate level $10^{-4} \, \text{s}^{-1} \leqslant \dot{\bar{\varepsilon}}^\text{p} \leqslant 100 \, \text{s}^{-1}$, Fig. 3

$$m = \frac{\text{d}(\bar{\sigma})}{\text{d}\log(\dot{\bar{\varepsilon}}^\text{p})}\bigg|_{\bar{\varepsilon}^\text{p},T} < 0 \quad \text{for } \dot{\bar{\varepsilon}}^\text{p} < \dot{\bar{\varepsilon}}^\text{p}_\text{trans} \tag{1}$$

* Corresponding author. Tel.: +33 3 87 31 50 20; fax: +33 3 87 34 42 79.
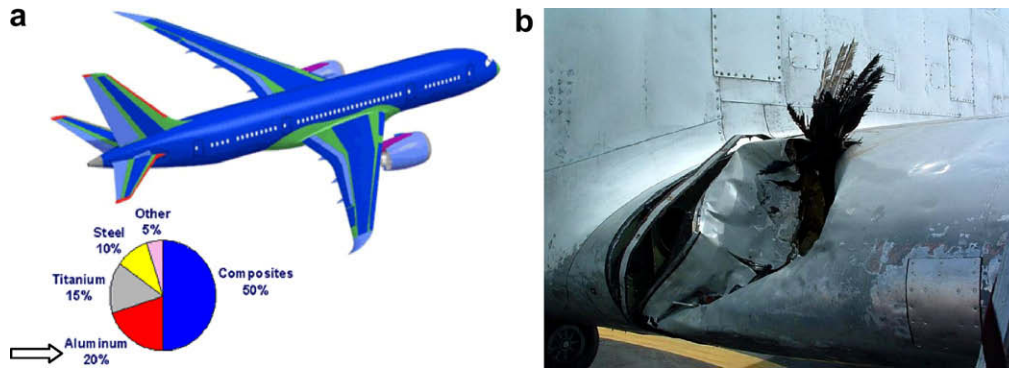*E-mail address:* rusinek@enim.fr (A. Rusinek).

Fig. 1. (a) Application of **AA** in aeronautical industry [2]. (b) Bird-impact test [3].
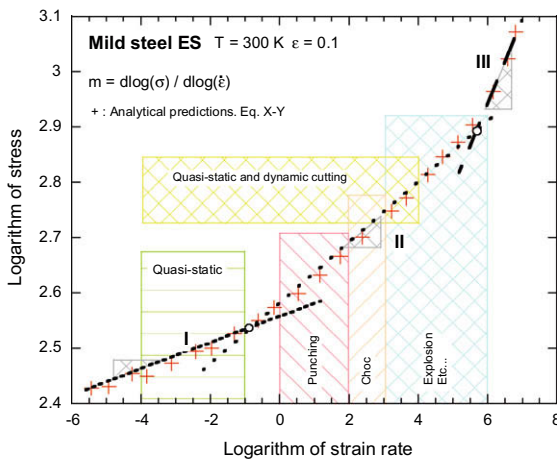

Fig. 2. Strain rate level associated to different industrial processes.

Such behaviour has considerable relevance in industrial applications since it may reduce the ductility of the material [5–7] and therefore affects to its formability and machinability. This effect called dynamic strain aging (**DSA**) was traditionally explained due to the solute–dislocation interaction at the microscopic level [8–11]. An alternative explanation has been proposed by Picu [12] and other authors based on the strength variation of dislocation junctions due to the presence of solute clusters on forest dislocations. At low strain rate, the solute has sufficient mobility to induce a clustering effect stopping mobile dislocations. At high rate

of deformation the increase of dislocations' velocity avoids appearance of clustering effect. Thus, beyond certain strain rate level $\dot{\varepsilon}_{trans}^{p}$, the strain rate sensitivity becomes positive, Fig. 3a. Moreover, since **DSA** is related to diffusion of solute, it is thermally activated [13,14]. The **NSRS** effect tends to disappear with decreasing temperature as it is shown in Fig. 3b for **AA 2024-T3**. Interesting studies concerning the effect of temperature on **DSA** are reported for example in [13,14].

Some attempts to model the **NSRS** are reported in the open literature, for example in [16–18]. The most relevant seems to be the approach due to McCormick [19].

However, such physical descriptions of **DSA** use to lead to complex mathematical formulations difficult to implement into **FE** codes. Moreover they use to have large number of material constants and difficult calibration-procedures. In addition, those models only define the material behaviour in the range of strain rate in which **DSA** takes place. They do not provide a formulation for the whole range of strain rates appearing in those engineering applications mentioned before, $10^{-4}\ \mathrm{s}^{-1} \leqslant \dot{\varepsilon}^{p} \leqslant 10^{4}\ \mathrm{s}^{-1}$.

2.2. The viscous-drag stress component taking place at high strain rates

In addition, a common characteristic of many **FCC** metals is the appearance of a viscous-drag component of the flow stress at high rate of deformation [20–22]. For strain rate level within the range $10^{3}\ \mathrm{s}^{-1} \leqslant \dot{\varepsilon}^{p} \leqslant 10^{4}\ \mathrm{s}^{-1}$ the flow stress sharply increases, Fig. 4.

Several explanations of this phenomenon have been proposed over the years. Most of them based on a transition in rate controlling deformation mechanism from thermal activation at low strain
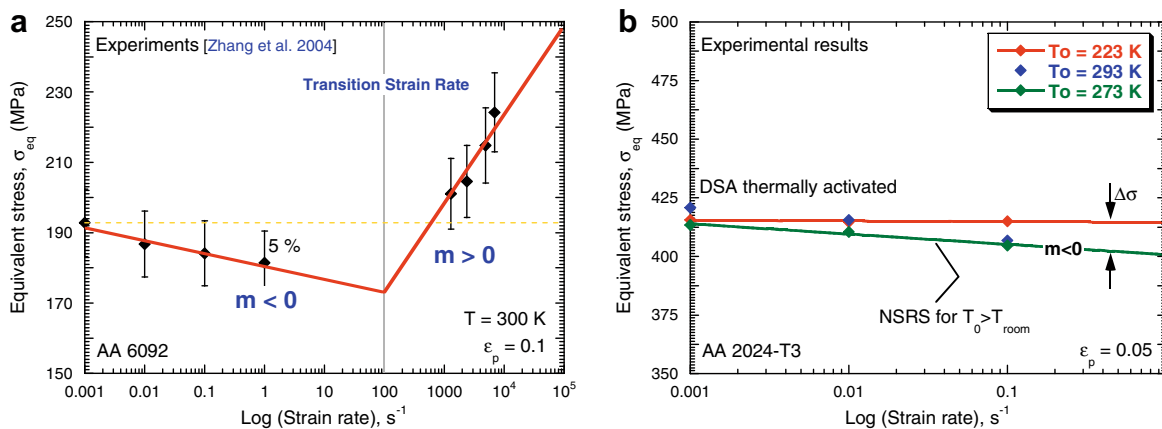

Fig. 3. (a) Description of the negative and positive strain rate sensitivities taking place in **AA 6092** [15]. (b) **DSA** dependence on initial temperature for **AA 2024-T3**.
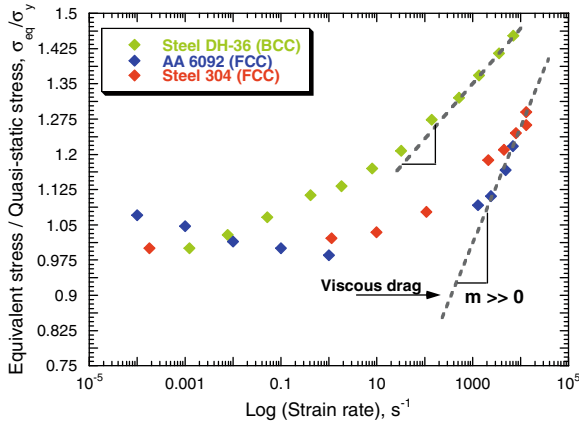
Fig. 4. Evolution of the normalized equivalent stress with strain rate for different **BCC** and **FCC** metals [15,20,23].

rates to some form of dislocations' drag [24–26]. According to Campbell and Ferguson [25] when the stress applied exceeds the barrier of the thermal activation, the time required to activate a dislocation past the short-range barriers of obstacles is negligible. Dislocation's velocity is controlled by dissipation of energy as it moves through the lattice. Assuming that this dissipation is of a linear viscous nature [25,27] the extra-stress (*applied stress–thermally activated stress–internal stress*) is approximately proportional to the strain rate and independent on temperature, Eq. (2b). In such a case the complete description of the flow stress should be decomposed in three components, Eq. (2a)

$$\bar{\sigma} = \sigma_\mu + \sigma^* + \sigma_{th} \tag{2a}$$
$$\sigma_{th} \approx \kappa \cdot \dot{\bar{\varepsilon}}^p \tag{2b}$$

where σ_μ is the internal stress which is related to the evolution of the microstructure, σ^* is the effective stress which describes the relation between strain rate and temperature, σ_{th} is the viscous-drag component and κ is a material constant.

Therefore, in the case of some **FCC** metals, the strain rate sensitivity cannot be defined using the physical models only based on the reciprocity between strain rate and temperature of Arrhénius equation.

2.3. Remarks on the modeling of aluminium alloys

Traditionally, constitutive relations as those due to Zerilli and Armstrong [28] or Johnson and Cook [29] have been used to describe the behaviour of **AA** and applied to simulate dynamic events, for example in [30–32]. However, they cannot define negative strain rate sensitivity, neither athermal flow stress due to viscous drag. Thus, the assumption of neglecting the strain rate sensitivity of **AA** has been a common practice during the last decades [30,32] when using the classical constitutive relations mentioned before. The structural relevance of aluminium components leads to the necessity of developing advanced constitutive models allowing for accurate definition of the **AA** behaviour at wide ranges of strain rate and temperature.

In the present paper an alternative for modeling the behaviour of **AA** at wide ranges of strain rate and temperature is presented. The models reported extend the original **RK** constitutive relation [33] to describe **NSRS** and viscous drag.

The extended **RK** models are used to define the thermo-viscoplastic behaviour of two commercial **AA** (*AA 5083-H116* and *AA 7075*) using experimental data available in the literature [1,34]. Their analytical results are compared with those obtained from the phenomenological constitutive relations reported in [1,34]. It

has been observed that the best agreement with experiments is achieved by the predictions provided by the extended **RK** constitutive relations. Moreover, the relations presented can be implemented into **FE** code using, for example, the algorithm proposed by Zaera and Fernandez-Saez [35].

3. The Rusinek–Klepaczko constitutive relation

The original formulation of the model is based on an additive decomposition of the total stress [36,37]. Thus, the stress is an addition of two terms σ_μ and σ^*, which define respectively the strain hardening and thermal the activation processes, Eq. 3. The first one is called internal stress and the second one effective stress. The term acting as multiplicative factor of the stresses addition $E(T)/E_0$ defines the Young's modulus evolution with temperature [38], Eq. 4

$$\bar{\sigma}(\bar{\varepsilon}^p, \dot{\bar{\varepsilon}}^p, T) = \frac{E(T)}{E_0}\left[\sigma_\mu(\bar{\varepsilon}^p, \dot{\bar{\varepsilon}}^p, T) + \sigma^*(\dot{\bar{\varepsilon}}^p, T)\right] \tag{3}$$

$$E(T) = E_0\left\{1 - \frac{T}{T_m}\exp\left[\theta^*\left(1 - \frac{T_m}{T}\right)\right]\right\} \tag{4}$$

where E_0, T_m and θ^* denote respectively the Young's modulus at $T = 0\,K$, the melting point and the characteristic homologous temperature. This expression allows for defining the thermal softening depending on the crystal lattice [39], Fig. 5. In the case of **FCC** metals (**AA** among others), $\theta^* \approx 0.9$ as it was reported in Rusinek at al. [39].

The internal stress is defined by Eq. 5

$$\bar{\sigma}_\mu(\bar{\varepsilon}^p, \dot{\bar{\varepsilon}}^p, T) = B(\dot{\bar{\varepsilon}}^p, T)(\varepsilon_0 + \bar{\varepsilon}^p)^{n(\dot{\bar{\varepsilon}}^p, T)} \tag{5}$$

where the modulus of plasticity B defines rate and temperature sensitivities of strain hardening, n is the strain hardening exponent depending on strain rate and temperature and ε_0 is the strain level which defines the yield stress at specific strain rate and temperature.

The explicit formulations describing the modulus of plasticity and the strain hardening exponent are given, Eqs. (6), (7)

$$B(\dot{\bar{\varepsilon}}^p, T) = B_0\left(\left(\frac{T}{T_m}\right)\log\left(\frac{\dot{\varepsilon}_{max}}{\dot{\bar{\varepsilon}}^p}\right)\right)^{-\nu} \tag{6}$$

$$n(\dot{\bar{\varepsilon}}^p, T) = n_0\left\langle 1 - D_2\left(\frac{T}{T_m}\right)\log\frac{\dot{\bar{\varepsilon}}^p}{\dot{\varepsilon}_{min}}\right\rangle \tag{7}$$

where B_0 is the material constant, ν is the temperature sensitivity, n_0 is the strain hardening exponent at $T = 0\,K$, D_2 is the material con-
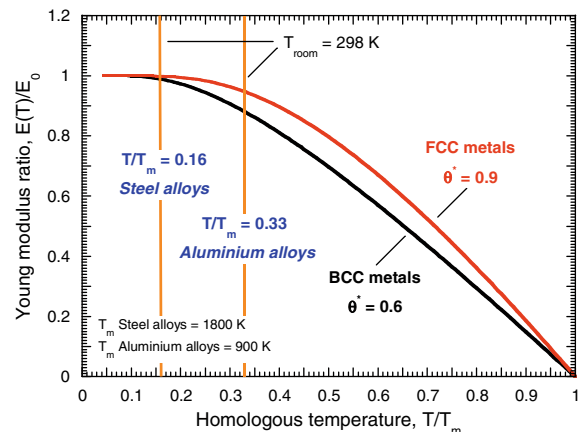

Fig. 5. Evolution of Young's modulus ratio for different θ^* values.

stant and $\dot{\varepsilon}^{\min}$ is the lower limit of the model. The McCauley operator $\langle \bullet \rangle = \bullet$ if $\langle \bullet \rangle \geqslant 0$ or $\langle \bullet \rangle = 0$ if $\langle \bullet \rangle \leqslant 0$.

The effective stress is obtained using Arrhénius relation which couples temperature with strain rate, Eq. 8

$$\sigma^*(\dot{\varepsilon}^p, T) = \sigma_0^* \left\langle 1 - D_1 \left(\frac{T}{T_m}\right) \log \left(\frac{\dot{\varepsilon}_{\max}}{\dot{\varepsilon}^p}\right) \right\rangle^{m^*} \tag{8}$$

where σ_0^* is the effective stress at $T = 0$ K, D_1 is the material constant, $\dot{\varepsilon}^{\max}$ is the maximum strain rate accepted for a particular material and m^* is the constant allowing to define the strain rate-temperature dependency [40].

Based on the experimental observations reported in [1,34] we assume that the rate controlling deformation mechanisms of the **AA** considered in this work are hardly dependent on plastic strain. Plastic strain does not influence rate and temperature sensitivities of the material, Eq. 8. Such consideration may not be valid for some other **FCC** metals as for example annealed copper [41].

As it was previously introduced, using the original **RK** formulation some particular aspects concerning the thermo-viscoplastic behaviour of **AA** cannot be defined accurately. Thus, in the following sections of the present paper two extensions of the **RK** model are presented. They define respectively the **NSRS** and the viscous drag that may be exhibited by **AA** under certain loading conditions.

4. Extension of RK model for defining negative strain rate sensitivity

In this section of the paper an extension of the **RK** model to define the **NSRS** is reported.

4.1. Formulation of the constitutive relation

The extension is conducted by adding a new term to the equivalent Huber–Misses stress $\bar{\sigma}$. The updated formulation of the model is reported in Eq. 9

$$\bar{\sigma}(\bar{\varepsilon}^p, \dot{\bar{\varepsilon}}^p, T) = \frac{E(T)}{E_0} \left[\sigma_\mu(\bar{\varepsilon}^p, \dot{\bar{\varepsilon}}^p, T) + \sigma^*(\dot{\bar{\varepsilon}}^p, T) + \sigma_{ns}(\dot{\bar{\varepsilon}}^p, T) \right] \tag{9}$$

where $\sigma_{ns}(\dot{\bar{\varepsilon}}^p, T)$ is the stress component accounting for the **NSRS** which is dependent on strain rate and temperature. This formulation has a semi-physical character and it is based on the experimental observations reported for example in [5,13,14]. The original expression proposed is defined by Eq. 10

$$\sigma_{ns}(\dot{\bar{\varepsilon}}^p, T) = \sigma_0^{ns} \cdot \left\langle \log \left(\frac{\dot{\bar{\varepsilon}}_{trans}}{\dot{\bar{\varepsilon}}^p}\right) \right\rangle \cdot \left\langle 1 - D_3 \left(\frac{T_m}{T}\right) \log \left(\frac{\dot{\bar{\varepsilon}}^p}{\dot{\bar{\varepsilon}}_{\max}}\right) \right\rangle \tag{10}$$

where σ_0^{ns} and D_3 are material constants describing respectively the stress decrease due to **DSA** and the reciprocity between strain rate and temperature. Such reciprocity is obtained using Arrhénius equation as it was reported previously for the effective stress $\sigma^*(\dot{\bar{\varepsilon}}^p, T)$. The influence of plastic strain in the **NSRS** effect is assumed negligible. Such assumption is based, for example, on the experimental data reported in [1]. Thus, in comparison with the original formulation of the **RK** relation just two new material constants are added. The transition between positive and negative strain rate sensitivity is denoted by $\dot{\bar{\varepsilon}}_{trans}^p$ and it can be obtained from experiments.

In the following curves is shown the evolution of the **NSRS** component, $\sigma_{ns}(\dot{\bar{\varepsilon}}^p, T)$ along with σ_0^{ns} and D_3 for different strain rate levels at room temperature $T_0 = 300$ K, Fig. 6. The value of the new stress component decreases with the strain rate increase, Fig. 6 until the transition strain rate level is reached (*it is considered $\dot{\bar{\varepsilon}}_{trans}^p = 76.58$ s^{-1}*). The increase of both material constants σ_0^{ns} and D_3 induces an augment on the **NSRS** of the material, Fig. 6.

In the case of adiabatic conditions of deformation the constitutive relation is combined with the energy balance principle, Eq. 11. Such relation allows for an approximation of the thermal softening of the material via the adiabatic heating

$$\Delta T(\bar{\varepsilon}^p, \dot{\bar{\varepsilon}}^p, \bar{\sigma}) = \frac{\beta}{\rho C_p} \int_0^{\bar{\varepsilon}_{\max}^p} \bar{\sigma} \, d\bar{\varepsilon}^p \tag{11}$$

where β is the Taylor–Quinney coefficient assumed as constant, ρ is the material density and C_p is the specific heat at constant pressure. Transition from isothermal to adiabatic conditions of deformation is assumed at $\dot{\bar{\varepsilon}}^p = 10$ s^{-1}, in agreement with experimental observations and numerical estimations reported for example in [42–44].

Subsequently is reported a straightforward method for calibration of the model parameters.

4.2. A systematic procedure for calculation of the model parameters

The procedure for calibration of the model is similar to that described in [45] for the original version of the **RK** constitutive relation. Thus, some details which are common for both models will be skipped in the explanation outlined below.

The main steps necessary for the definition of the model parameters are:

i. It is assumed that at low strain rate $\dot{\bar{\varepsilon}}_{reference}^p \leqslant 0.001$ s^{-1} and room temperature the stress contribution due to thermal activation can be neglected $\sigma^*(\dot{\bar{\varepsilon}}^p, T) = 0$. Under this assumption is possible to define the constant D_1.

ii. Subsequently, the transition strain rate $\dot{\bar{\varepsilon}}_{trans}^p$ at room temperature is identified for a given plastic strain value $\bar{\varepsilon}_p$. For the range of strain rate $\dot{\bar{\varepsilon}}^p \leqslant \dot{\bar{\varepsilon}}_{trans}^p$ the value of stress corresponding to $\dot{\bar{\varepsilon}}_{trans}^p$ is subtracted of the real flow stress level, Fig. 7. The stress difference is the flow stress decrease due to **NSRS** and it is fitted to Eq. 10 using the least square method. Thus, the material constants σ_0^{ns} and D_3 are obtained.

iii. The strain rate sensitivity of the model is artificially neglected in the range $\dot{\bar{\varepsilon}}_{reference}^p \leqslant \dot{\bar{\varepsilon}}^p \leqslant \dot{\bar{\varepsilon}}_{trans}^p$. In that range, the flow stress level is assumed to be that corresponding to $\dot{\bar{\varepsilon}}_{trans}^p$. Then is assumed that the increase of the total stress (*taking place for $\dot{\bar{\varepsilon}}^p \geqslant \dot{\bar{\varepsilon}}_{trans}^p$*) with the strain rate is due to the effective stress $\sigma^*(\dot{\bar{\varepsilon}}^p, T)$. Thus, the stress increase is defined as follows, Eq. 12

$$\Delta\sigma(\dot{\bar{\varepsilon}}_{reference}^p \rightarrow \dot{\bar{\varepsilon}}^p)|_{\bar{\varepsilon}^p} = \bar{\sigma}(\dot{\bar{\varepsilon}}^p)|_{\bar{\varepsilon}^p} - \bar{\sigma}(\dot{\bar{\varepsilon}}_{reference}^p)|_{\bar{\varepsilon}^p} = \sigma^*(\dot{\bar{\varepsilon}}^p, T)|_{\bar{\varepsilon}^p} \tag{12}$$

By combination of Eq. 8 with experimental results for an imposed strain level, $\bar{\varepsilon}_p$, is possible to determine the material constants m^* and σ_0^*. For the steps ii and iii, the strain level should be assumed $\bar{\varepsilon}^p \leqslant 0.1$ in order to guarantee isothermal condition of deformation. For larger strain values, adiabatic condition induces a thermal softening of the material and in such case a decrease of the strain hardening rate.

iv. The last step is application of the complete equation for the total stress, Eq. 9. combined with experimental results, $\bar{\sigma} - \bar{\varepsilon}^p|_{\dot{\bar{\varepsilon}}^p}$. Then the stress dependency upon temperature and strain rate for the modulus of plasticity B and the strain hardening exponent n can be defined.

4.3. Application to AA 5083-H116

The **AA** 5xxx series are alloyed with magnesium, derive most of their strength from solution hardening, and can also be work hardened to strengths comparable to steel alloys. **AA 5083-H116** is one
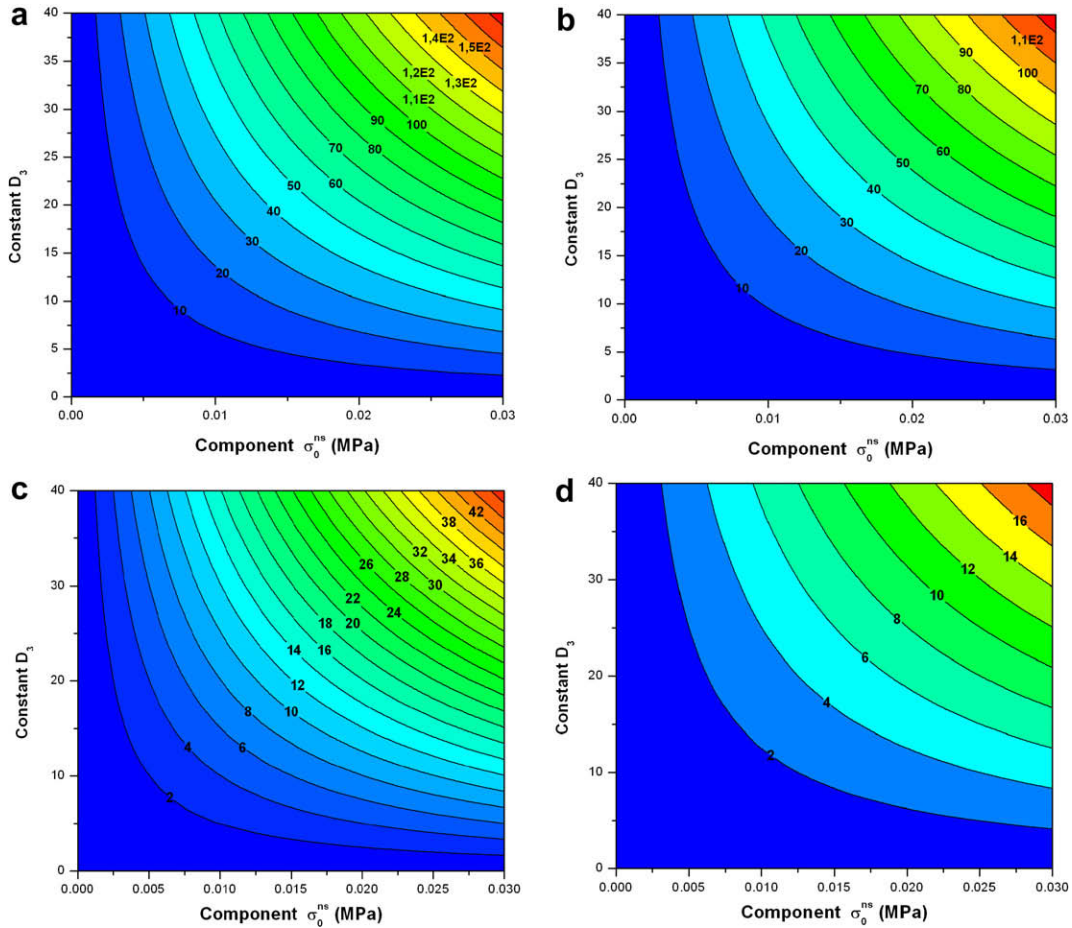
Fig. 6. Evolution of the negative strain rate component with σ_0^{ns} and D_3 for different strain rate levels at room temperature. (a) 0.001 s^{-1}, (b) 0.01 s^{-1}, (c) 1 s^{-1}, (d) 10 s^{-1}.
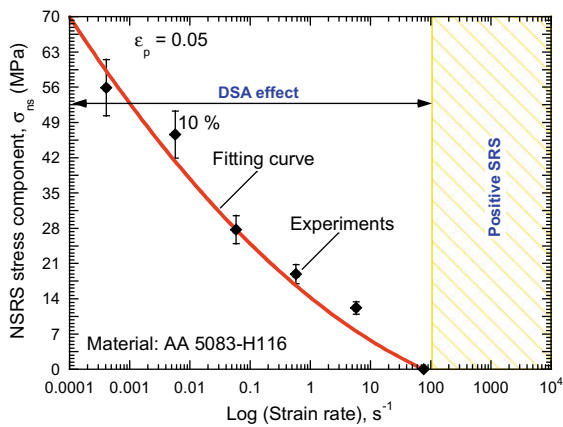

Fig. 7. Calibration of the **NSRS** for **AA 5083-H116** using the experimental data reported in [1].

of the strongest aluminium–magnesium alloys. It is widely used in naval structures as ship hulls and offshore topsides due to its high strength and good corrosion resistance. The main alloying elements are listed in Table 1.

The high content of magnesium is responsible of the **NSRS** showed by this **AA** as it was discussed in [1,47].

Using the procedure reported in the previous section, the model has been calibrated for **AA 5083-H116** using the experimental data reported in [1]. The following set of constants has been found, Tables 2 and 3.

Table 1
Chemical composition of **AA 5083-H116** (% of wt) [46].

Mn	Si	Cr	Ti	Fe	Mg	Zn	Ti	Cu
0.5	0.4	0.17	0.15	0.5	4.5	0.25	0.2	0.1

Conventional physical constants of **AA** can be obtained from material handbooks, Table 4.

Since the maximum strain rate reported in the experiments taken as reference is $\dot{\varepsilon} \approx 1000$ s^{-1} [1] it is assumed that the viscous drag is not active [22]. Thus, the contribution of a potential viscous-drag component to the flow stress for the range of strain rates considered can be neglected.

Next, the predictions of the extended **RK** model are validated with experiments.

4.4. Validation of the extended RK constitutive relation for modeling the thermo-viscoplastic behaviour of AA 5083-H116 and comparison with the modified JC model

The first step is to evaluate the definition of the **NSRS** provided by the extended **RK** model proposed. In Fig. 8 is shown the agreement between analytical predictions and experiments for different strain rates 0.00041 s$^{-1} \leqslant \dot{\varepsilon} \leqslant 122$ s^{-1}. The lower limit $\dot{\varepsilon}^p = 0.00041$ s^{-1} corresponds to the minimum value of strain rate for which there are experimental data available. The upper limit is approximately the strain rate value corresponding to the transition between the negative and the positive strain rate sensitivity

Table 2
Constants determined for **AA 5083-H116** for **RK** model, Eq. 3.

B_0 (MPa)	v (−)	n_0 (−)	D_2 (−)	ε_0 (−)	σ_0^* (MPa)	m^* (−)	D_1 (−)	T_m (K)	$\dot{\varepsilon}_{min}$ (s^{-1})	$\dot{\varepsilon}_{max}$ (s^{-1})
666	0.01	0.35	0.04	0.0118	1536.3	8.37	0.3	900	10^{-5}	10^7

Table 3
Constants determined for **AA 5083-H116** for extension of **RK** model to **NSRS**, Eq. 10.

σ_0^{ns} (MPa)	D_3 (−)	$\dot{\varepsilon}_{trans}^{p}$ (s^{-1})
0.01	36	76.58

Table 4
Physical constants for **AA**.

E_0 (MPa)	θ^* (−)	C_p (J kg K^{-1})	β (−)	ρ (kg m^{-3})
70	0.9	900	0.9	2700

Fig. 9. Temperature sensitivity description using extended **RK** model and comparison with experiments for $\varepsilon^p = 0.045$ and 0.00017 s^{-1} [1].

$\dot{\bar{\varepsilon}}^p = 122 \text{ s}^{-1} \approx \dot{\bar{\varepsilon}}_{trans}^p = 76.58 \text{ s}^{-1}$. Thus, the flow stress level in the case of $\dot{\bar{\varepsilon}}^p = 122 \text{ s}^{-1} \approx \dot{\bar{\varepsilon}}_{trans}^p$ is lower than in the case of $\dot{\bar{\varepsilon}}^p = 0.00041 \text{ s}^{-1}$. Therefore, such a good agreement for the range of strain rate considered means that the model is describing correctly the **DSA** effect.

Concerning the temperature sensitivity, the experimental data available just allow for evaluating the model in the case of $T \geqslant T_{room}$, Fig. 9. The model describes accurately the decrease of the flow stress with temperature Fig. 9. The difference is only found in the case of $T = 600$ K.
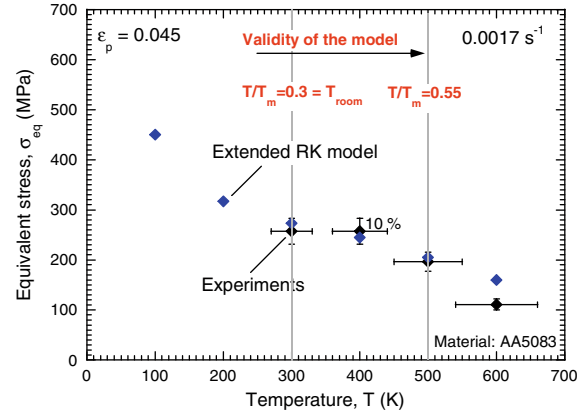
Subsequently, the analytical predictions of the extended **RK** model are compared with those corresponding to the modified Johnson–Cook (**MJC**) model reported in [1]. The **MJC** defines the Huber–Misses stress as a multiplicative law of three uncoupled
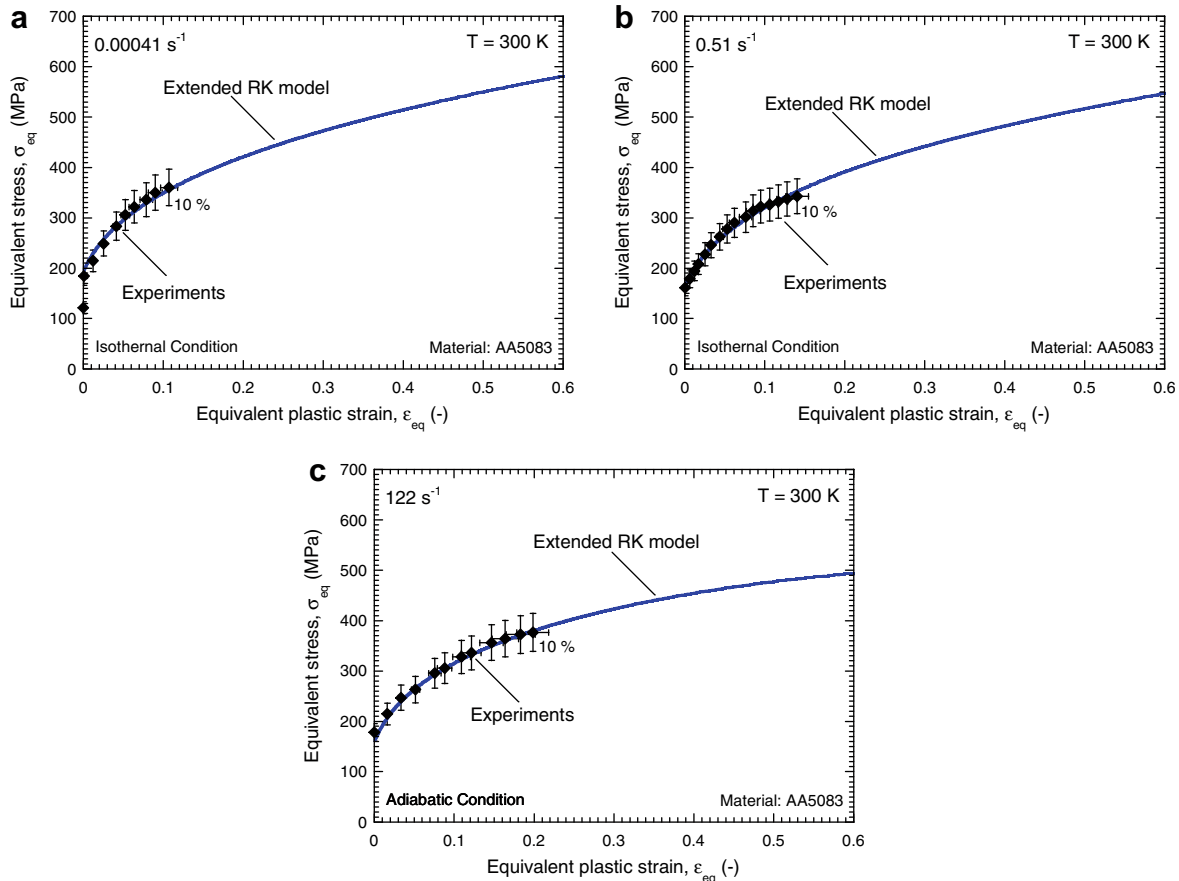

Fig. 8. **NSRS** description using extended **RK** model and comparison with experiments at room temperature [1]. (a) 0.00041 s^{-1}, (b) 0.51 s^{-1}, (c) 122 s^{-1}.

Table 5
Constants determined for **AA 5083-H116** for **MJC** model [1].

A (MPa)	B (MPa)	n (–)	C (–)	m (–)	T_0 (K)	T_m (K)	$\dot{\varepsilon}_0$ (s^{-1})
167	596	0.551	0.001	0.859	296	900	0.0005

terms. Those terms are respectively dependent on plastic strain $\bar{\varepsilon}^p$, strain rate $\dot{\bar{\varepsilon}}^p$ and temperature T, Eq. 13:

$$\sigma(\bar{\varepsilon}^p, \dot{\bar{\varepsilon}}^p, T) = (A + B \cdot (\bar{\varepsilon}^p)^n) \cdot \left(1 + \frac{\dot{\bar{\varepsilon}}^p}{\dot{\varepsilon}_0}\right)^C \cdot \left(1 - \left(\frac{T - T_0}{T_m - T_0}\right)^m\right) \quad (13)$$

where A is the quasi-static yield stress at $\dot{\bar{\varepsilon}}^p = \dot{\varepsilon}_0$ and T = const., B is the modulus of strain hardening, n is the strain hardening exponent, C is the material constant defining the strain rate sensitivity and $\dot{\varepsilon}_0$ is the strain rate of reference. Moreover T is the current temperature, T_0 is the reference temperature, T_m is the melting point and m defines the temperature sensitivity.

Several comments must be done concerning this constitutive relation. Strain hardening is defined as a power law, so called Swift hardening, but without taking into account the effect of strain rate and temperature. The constancy of the strain hardening exponent n in the formulation is contrary to the observations frequently made and reported for metals in many publications, for example [45,48]. This fact raises considerable relevance, especially in dynamic events susceptible for plastic instabilities, [45].

In comparison with the original **JC** model, this modified version tries to improve the definition of the strain rate sensitivity. In the **MJC** the constant-logarithmic definition proposed by the original version of the **JC** model is replaced by a power law. However, such kind of approach is still ineffective to define the material behaviour for wide ranges of strain rate as it was discussed by Rusinek et al. [4]. Moreover, the **MJC** model (*as well as the original JC formulation*) holds an important disadvantage in comparison with the extended **RK** relation. It is needed of three mechanical tests at different initial temperatures to be calibrated. In the case of the extended **RK** model (*as well as the original RK formulation*) the temperature sensitivity is automatically obtained from the reciprocity strain rate/temperature of Arrhénius equation.

The **MJC** model constants reported for **AA 5083-H116** in [1] are shown in Table 5.

The **MJC** constitutive relation is not able to define the behaviour of this material from quasi-static to high strain rate level. Thus, the authors [1] decided to neglect the strain rate sensitivity of the material $C \approx 0$. It avoids definition of the **NSRS** up to intermediate strain rate level $\dot{\bar{\varepsilon}}^p \approx 100$ s^{-1} as well as the positive strain rate sensitivity beyond that point.

In the following plot, Fig. 10, experimental data are compared with analytical predictions of both models for two different strain rate levels at room temperature. In the case of $\dot{\bar{\varepsilon}}^p = 3.95$ s^{-1} the predictions of the extended **RK** model fit correctly the experimental data. The **MJC** overestimates the flow stress and the strain hardening of the material. In the case of $\dot{\bar{\varepsilon}}^p = 1313$ s^{-1}, both models offer predictions close to the experimental data and the thermal softening due to adiabatic heating is well defined.

In order to obtain a complete description of the strain rate sensitivity predicted by both models the following plots are reported, Fig. 11. The analytical predictions of the flow stress evolution along the strain rate are compared with experiments. Several comments are outlined below:

i. The predictions using the extended **RK** model, Eq. 9 define correctly the strain rate sensitivity of the material in the range of strain rates considered. Both, the negative and the positive strain rate sensitivities exhibited by the material are accurately described.

ii. The predictions of the **MJC** model neither account for the negative, nor the positive, strain rate sensitivity of the material. In addition, when the adiabatic heating at high strain rates is taken into account, the reduced value of the constant $C \approx 0$ leads to an artificial decrease of the flow stress along the whole range of strain rates considered. Such description of the material behaviour lacks of physical meaning.

iii. The **MJC** model only shows satisfactory agreement with experiments in a reduced range of strain rates 300 s$^{-1} \leqslant \dot{\bar{\varepsilon}}^p \leqslant 1500$ s^{-1}. It induces erroneous definition of the material behaviour.

In the following section of the paper the is reported the extension of **RK** model for modeling viscous drag at high strain rates.

5. Extension of RK model for defining viscous-drag stress at high strain rates

In this section of the paper is presented an extension of the **RK** model to define the viscous drag taking place in some **FCC** metals when subjected to high rate of deformation as it was reported in [20–22,26,49,50].
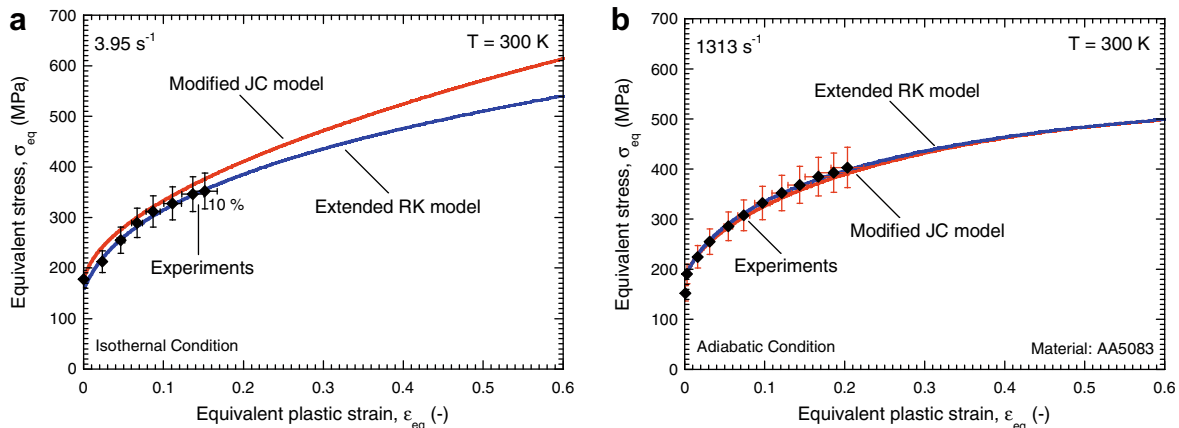

Fig. 10. Description of the flow stress evolution along plastic strain using extended **RK** and **MJC** models and comparison with experiments at room temperature [1]. (a) 3.95 s^{-1},[1] (b) 1313 s^{-1}.
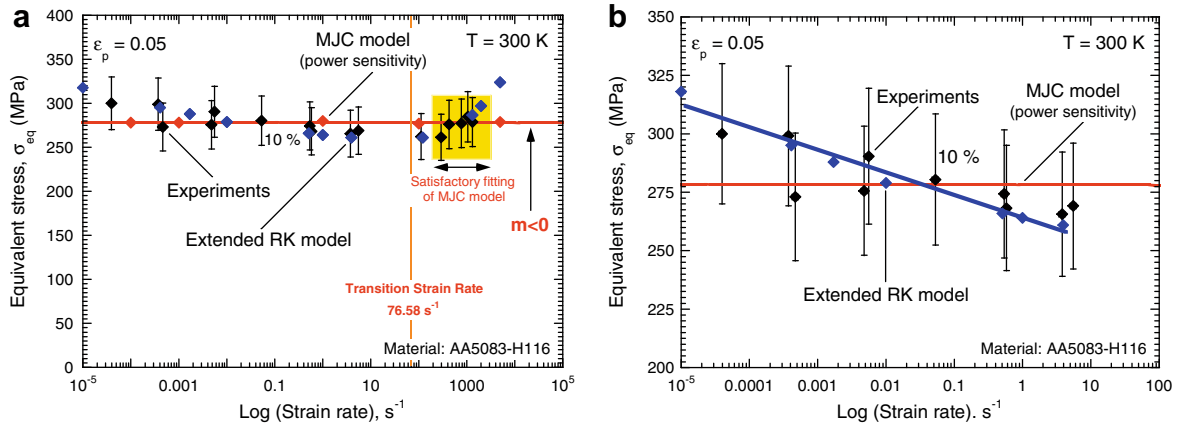
Fig. 11. Description of the flow stress evolution along strain rate using extended **RK** and **MJC** models and comparison with experiments at room temperature and $\varepsilon^p = 0.05$ [1]. (a) Complete range of strain rates and (b) detail of **DSA** effect.

5.1. Formulation of the constitutive relation

The extension is conducted adding a new term to the equivalent Huber–Misses stress $\bar{\sigma}$. The updated formulation of the model is reported in Eq. 14:

$$\bar{\sigma}(\bar{\varepsilon}^p, \dot{\bar{\varepsilon}}^p, T) = \frac{E(T)}{E_0}\left[\sigma_\mu(\bar{\varepsilon}^p, \dot{\bar{\varepsilon}}^p, T) + \sigma^*(\dot{\bar{\varepsilon}}^p, T)\right] + \sigma_{ath}(\dot{\bar{\varepsilon}}^p) \tag{14}$$

where $\sigma_{ath}(\dot{\bar{\varepsilon}}^p)$ is the stress component accounting for the viscous drag which is just dependent on strain rate as it was discussed in [22]. In comparison with the **NSRS** component, this new term is not multiplied by the dependency of the Young's modulus with temperature.

The formulation used to define the viscous-drag component $\sigma_{ath}(\dot{\bar{\varepsilon}}^p)$ was originally introduced in [22,51,52] and it has a semi-physical character. It comes from the proven relation between viscous drag and strain rate given by Eq. 15 [51]:

$$\sigma_{ath} \approx \sigma_{ath}\left(\left(\frac{M^2 \cdot B}{\rho_m \cdot b^2}\right), \dot{\bar{\varepsilon}}^p\right) \propto \dot{\bar{\varepsilon}}^p \tag{15}$$

where M is the Taylor factor, B is the drag coefficient, ρ_m is the mobile dislocation density and b is the magnitude of the Burgers vector.

Thus, based on experimental observations, Kapoor and Nemat-Nasser [22] set the following relations, Eqs. (16a) and (16b)
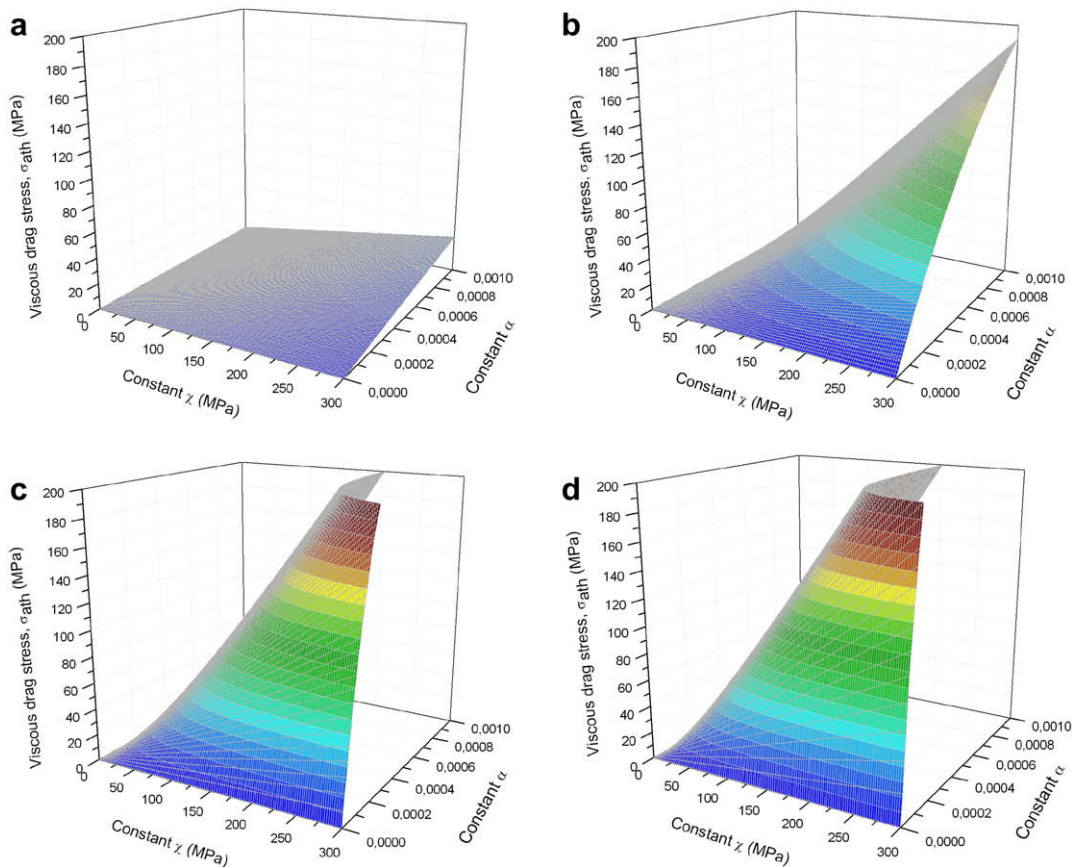

Fig. 12. Evolution of the viscous-drag component with χ and α for different strain rate levels. (a) 100 s^{-1}, (b) 1000 s^{-1}, (c) 5000 s^{-1}, (d) $10,000 \text{ s}^{-1}$.

$$\sigma_{ath}(\dot{\bar{\varepsilon}}^p) = \chi \cdot \left[1 - \exp\left(-\alpha \cdot \dot{\bar{\varepsilon}}^p\right)\right] \propto \dot{\bar{\varepsilon}}^p \qquad (16a)$$

$$\alpha = \left(\frac{M^2 \cdot B}{\rho_m \cdot b^2 \cdot \tau_y}\right) \qquad (16b)$$

where χ is a material constant, α represents an effective damping coefficient affecting the dislocation motion and τ_y is a high temperature yield stress [51,52]. The value of the constants χ and α can be obtained directly from experiments [51,52].

In the following curves is shown the evolution of the viscous-drag component along with χ and α for different strain rate levels, Fig. 12. Under a certain level of deformation rate $\dot{\bar{\varepsilon}}^p \leqslant 1000 \text{ s}^{-1}$ the viscous-drag component is negligible no matter the value of the constants χ and α, Fig. 12. In that case, the rate sensitivity is governed by the thermal activation mechanisms.

At higher strain rate level $\dot{\bar{\varepsilon}}^p \geqslant 1000 \text{ s}^{-1}$ the flow stress due to viscous drag becomes relevant and it quickly increases with the rate of deformation, Fig. 12. The increase of both material constants χ and α induces an augment on the flow stress.

As reported for the extension of the **RK** model to the **NRSR**, this constitutive relation is combined with the energy balance principle, Eq. 11 in the case of adiabatic conditions of deformation, $\dot{\bar{\varepsilon}}^p \geqslant 10 \text{ s}^{-1}$.

5.2. A systematic procedure for calculation of the model parameters

As reported for the previous model, the procedure for calibration of the constitutive relation is similar to that defined for the original version of the **RK** [45].

The main steps necessary for identification of the model parameters are:

i. The first step is equivalent to the step i reported for the previous model.
ii. For **FCC** metals, the strain rate sensitivity in the strain rate range controlled by the thermally activated deformation mechanisms is of the type $\bar{\sigma} \propto \log(\dot{\bar{\varepsilon}}^p)$ [20,24–26]. Such sensitivity drastically changes when viscous drag deformation mechanisms take place. Then, the relation $\bar{\sigma} \propto \dot{\bar{\varepsilon}}^p$ is fulfilled as previously reported. Transition strain rate level $\dot{\bar{\varepsilon}}^p_{trans-drag}$ from thermally activated deformation mechanisms to viscous drag has to be identified from experiments. Then, for the range $\dot{\bar{\varepsilon}}^p \leq \dot{\bar{\varepsilon}}^p_{trans-drag}$ Eq. 8 is applied and the values of m^* and σ_0^* are identified.
iii. In the case of $\dot{\bar{\varepsilon}}^p_{trans-drag} \leqslant \dot{\bar{\varepsilon}}^p$ the stress difference between model predictions (*without viscous-drag component*) and experiments is due to the athermal term $\sigma_{ath}(\dot{\bar{\varepsilon}}^p)$, Fig. 13. By combination of Eq. (16a) with experimental results for an imposed strain level, $\bar{\varepsilon}^p$, is possible to determine the material constants χ and α, Fig. 13.
iv. The last step is equivalent to the step 4 reported for the previous model.

5.3. Application to AA 7075

The **AA** 7xxx series are alloyed with zinc, and can be hardened to the highest strengths of any **AA**. **AA 7075** notable for its strength, with good fatigue strength and average machinability, but it is not weldable and has less resistance to corrosion than many other **AA**. It is widely used in aeronautical industry for construction of aircraft structures, such as wings and fuselages. Its main alloying elements are listed in Table 6.

Using the procedure reported in the previous section, the model has been calibrated for **AA 7075** using the experimental data reported in [34]. The following set of constants has been found, Tables 7 and 8.

In the following section, the predictions of the extended **RK** model are compared with experiments.

5.4. Validation of the extended RK constitutive relation for modeling the thermo-viscoplastic behaviour of AA 7075 and comparison with a phenomenological model

The first step is to evaluate the predictions of the extended **RK** model for different strain rate levels. It is reported in Fig. 14 a satisfactory agreement between the model and the experiments from quasi-static loading to high strain rate $0.001 \text{ s}^{-1} \leqslant \dot{\bar{\varepsilon}}^p \leqslant 2529 \text{ s}^{-1}$. The difference only takes place after saturation stress stage $d\bar{\sigma}/d\bar{\varepsilon}^p = 0$ which corresponds to non-homogeneous behaviour (*open symbols in* Figs. 14, 16, 17 and 19). In such a case nucleation and growth of micro voids sharply decrease the flow stress, Fig. 15 [34]. It must be noticed that the viscous-drag component added to
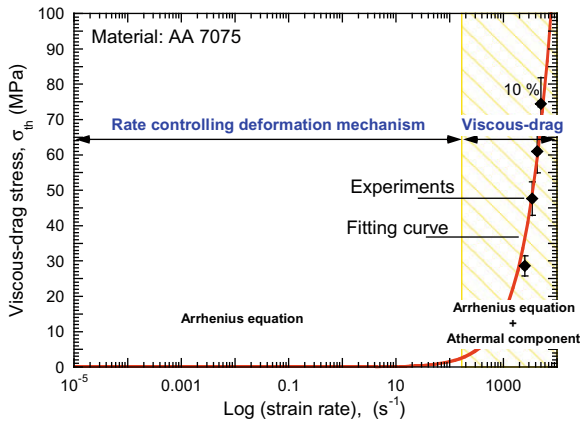

Fig. 13. Calibration of the viscous-drag stress component for **AA 7075** using experimental data reported in [34].

Table 6
Chemical composition of **AA 7075** (% of wt) [53].

Mn	Si	Cr	Ti	Fe	Mg	Zn	Ti	Cu
0.3	0.4	0.23	0.2	0.5	2.5	5.5	0.2	1.6

Table 8
Constants determined for **AA 7075** for the viscous-drag component of the extended **RK** model, Eq. (16a).

χ (MPa)	α (−)
286.7	0.00005368

Table 7
Constants determined for **AA 7075** for **RK** model, Eq. 3.

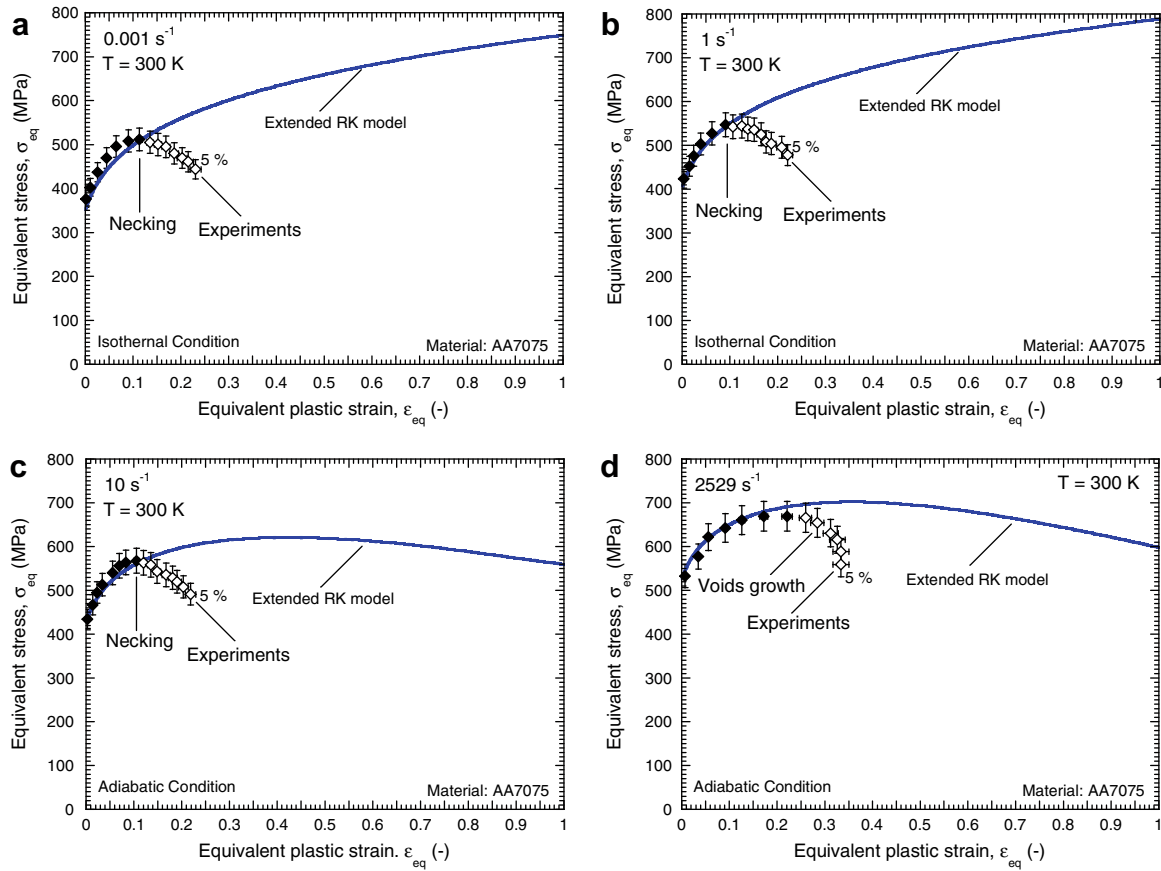| B_0 (MPa)	v (−)	n_0 (−)	D_2 (−)	ε_0 (−)	σ_0^* (MPa)	m^* (−)	D_1 (−)	T_m (K)	$\dot{\varepsilon}_{min}$ (s^{-1})	$\dot{\varepsilon}_{max}$ (s^{-1})
790.3	−0.0002	0.1966	0.0555	0.018	196.57	1.2857	0.3	900	10^{-5}	10^7

Fig. 14. Description of the flow stress evolution along with plastic strain using extended **RK** model and comparison with experiments at room temperature [34]. (a) 0.001 s^{-1}, (b) 1 s^{-1}, (c) 10 s^{-1}, (d) 2529 s^{-1}.
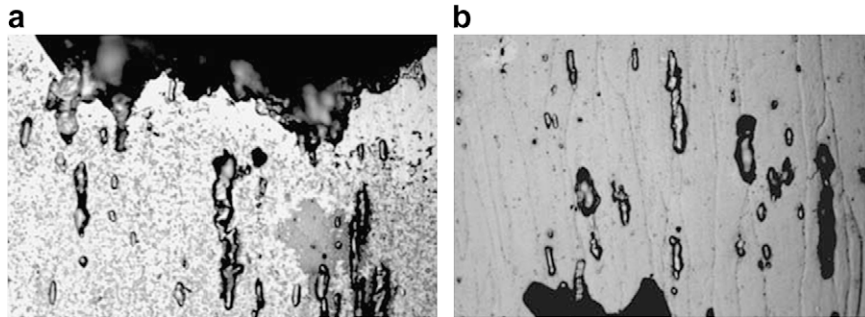

Fig. 15. Optical micrographs of tested specimens. Damage induced by voids growth. (a) 0.001 s^{-1} T = 300 K [34], (b) 10 s^{-1} T = 500 K [34].

the **RK** model allows for correct definition of the material behaviour at high rate of deformation, Fig. 14d.

The viscous-drag component exhibits great relevance on the description of the material behaviour when subjected to elevated initial temperature and high rate of deformation. It compensates the underestimation on the flow stress at high strain rate that would be obtained using just the Arrhenius equation as mechanism to describe the rate sensitivity of the material, Fig. 16b. That point is confirmed in Fig. 16 where the analytical predictions of the original formulation of the **RK** model are compared with those corresponding to the extension introduced in the present paper.

The analytical predictions of the extended **RK** constitutive relation for **AA 7075** are compared with those corresponding to the phenomenological model (**PM**) reported in [34]. El-Magd [54] proposed a multiplicative model taking into account strain hardening $\bar{\varepsilon}^{\mathrm{p}}$ and strain rate $\dot{\bar{\varepsilon}}^{\mathrm{p}}$ and temperature T sensitivities, Eq. 17

$$\bar{\sigma}(\bar{\varepsilon}^{\mathrm{p}}, \dot{\bar{\varepsilon}}^{\mathrm{p}}, T) = \left[[K \cdot (B + \bar{\varepsilon}^{\mathrm{p}})^n + \eta \cdot \dot{\bar{\varepsilon}}^{\mathrm{p}}] \cdot \exp\left(-\beta \cdot \left(\frac{T - T_0}{T_{\mathrm{m}}} \right) \right) \right] \quad (17)$$

where B, K, and n are material constants defining strain hardening. The strain hardening coefficient K, as well as the strain hardening exponent n, is not dependent on strain rate and temperature. Thus, it is avoided an accurate prediction of the thermal softening of the material at high strain rates. The strain rate sensitivity is defined by the material constant η. The relation $\bar{\sigma} \propto \eta \cdot \dot{\bar{\varepsilon}}$ answers to experimental observations reported for example in [20,25]. Such formulation of the strain rate sensitivity is only valid for defining viscous drag effect at high rate of deformation. It is ineffective to model the behaviour of the material at wide ranges of strain rate. Moreover, T_{m} is the melting temperature, T_0 is the temperature of reference and β is a material constant defining the temperature sensitivity.
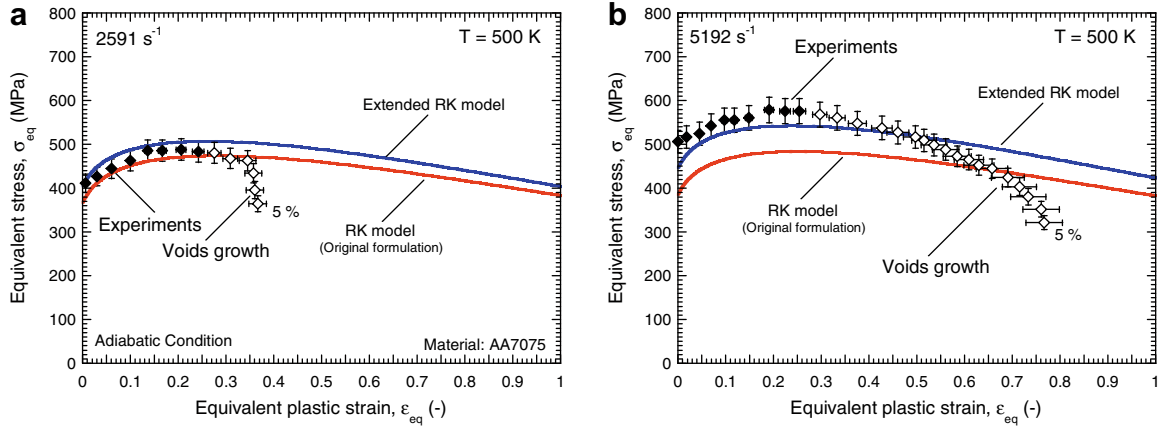
Fig. 16. Description of the flow stress evolution along plastic strain using **RK** and extended **RK** models and comparison with experiments at $T_o = 500$ K [34]. (a) 2591 s^{-1}, (b) 5192 s^{-1}.
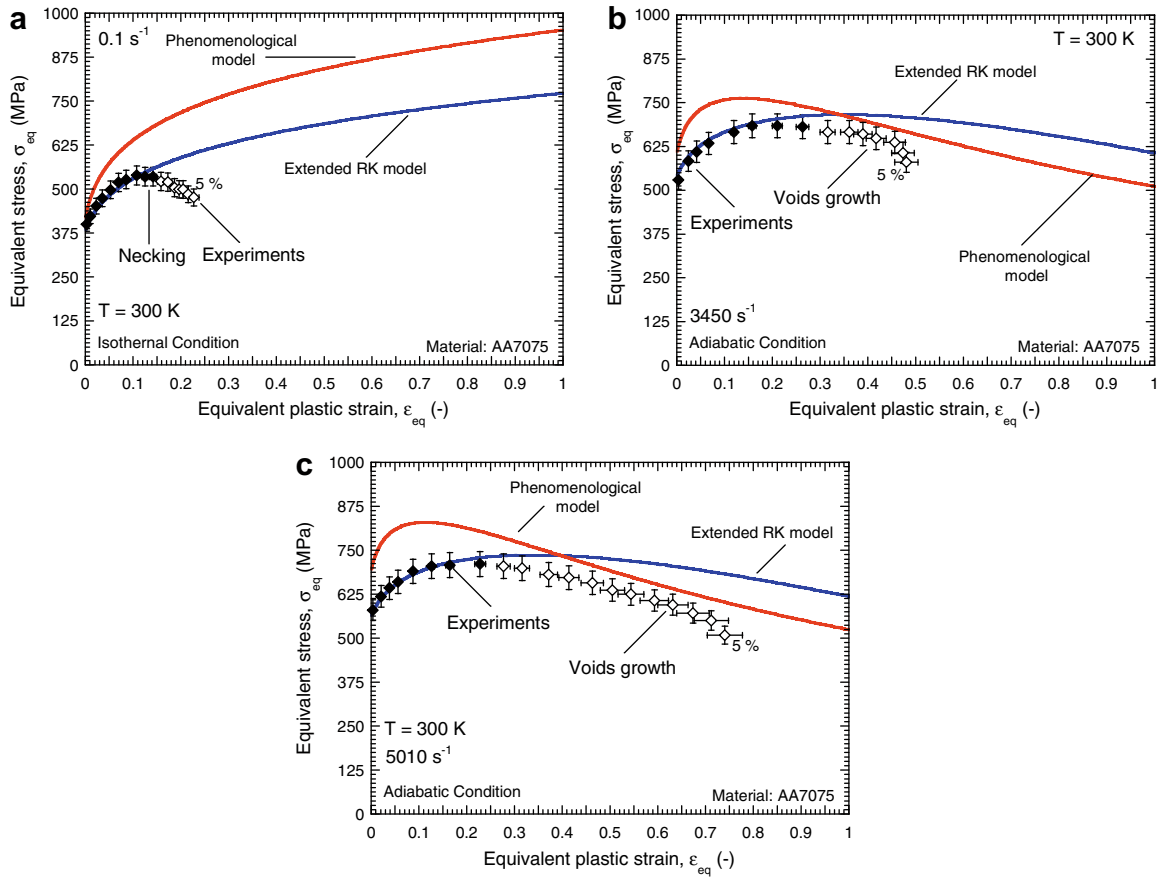

Fig. 17. Description of the flow stress evolution along plastic strain using extended **RK** and modified **PM** models and comparison with experiments at room temperature [34]. (a) 0.1 s^{-1},[1] (b) 3450 s^{-1}, (c) 5010 s^{-1}.

As previously reported for the **MJC** relation, the **PM** model is needed of larger number of experimental test to be calibrated in comparison with the extended **RK** constitutive law.

The following **PM** model constant-values are reported in [34] for **AA 7075**, Table 9.

In the following plot, Fig. 17, the experimental data are compared with the analytical predictions of both models for three different strain rate levels at room temperature. At low strain rate $\dot{\varepsilon}^p = 0.1$ s^{-1}, Fig. 17a. the **PM** model strongly overestimates the flow stress as well as the strain hardening of the material. At high

rate of deformation the **PM** model also overestimates the flow stress and the strain hardening but just until a certain value of plastic strain is reached, Fig. 17b and c. After that level of plastic strain the flow stress suddenly starts to decrease and it becomes lower than that predicted by the extended **RK** model. As it was previously reported, the strong decrease of the flow stress after saturation is due to material damage and not due to thermal softening. Such decrease should not be defined by the constitutive relation but by a damage model since damage corresponds to non-homogeneous behaviour of the material.
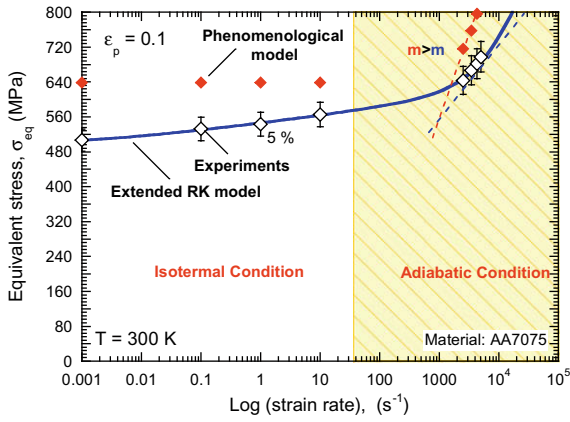
Fig. 18. Description of the flow stress evolution along strain rate using extended **RK** and **PM** models and comparison with experiments at room temperature and $\varepsilon^p = 0.1$ [34].

Table 9
Constants determined for **AA 7075** for phenomenological model [34].

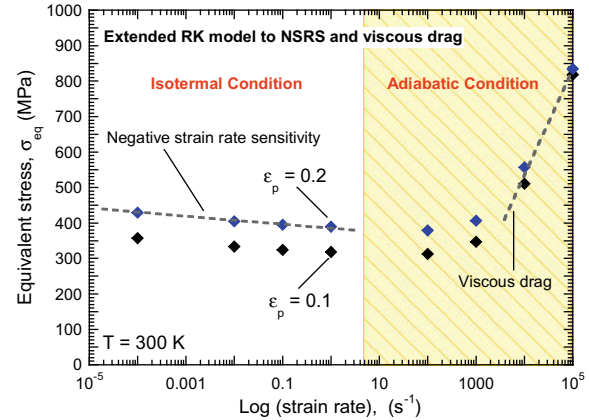| K (MPa)	B (–)	n (–)	η (MPa s)	a (MPa/s)	β (–)	T_0 (K)	T_m (K)
960	0.01	0.18	0.0555	0.00115	3	296	900

Fig. 20. Description of the flow stress evolution along strain rate using extended **RK** model to negative strain rate sensitivity and viscous drag (analytical predictions for an artificial material using the constants of Tables 2–4 and 8).

In the following plot, Fig. 18, the analytical predictions of **PM** and extended **RK** models concerning the flow stress evolution with strain rate are compared with experiments. Some comments are outlined below:

i. The predictions using extended **RK** model define correctly the strain rate sensitivity of the material in the range of strain rates considered. Both, the thermally activated flow stress and the viscous drag at high strain rates are accurately described.

ii. The **PM** model does not account for the thermally activated flow stress. The strain rate sensitivity it proposes just defines the linear relation between stress level and strain rate taking place at high strain rate. Even in the case of fast loading, the model overestimates the flow stress level.

The relevance of the definition of the viscous-drag stress component is apparent in the following plots, Fig. 19. With the increase of the initial temperature the **PM** model strongly underestimates the flow stress (*opposite behaviour to that reported at room temperature, Fig. 17*).

From this observation may be concluded that the use of multiplicative constitutive laws may lead to an inaccurate definition of the thermo-viscoplastic behaviour of **AA**.

6. Conclusion and remarks

In this paper are presented two extensions of the **RK** constitutive relation to define the behaviour of **AA**. The formulations reported expand the validity of the **RK** model to the definition of particular aspects of the behaviour of **AA**, namely the negative strain rate sensitivity and the viscous drag. The goal is to develop constitutive relations capable of defining accurately the thermoviscoplastic behaviour of **AA** at wide ranges of strain rate and temperature. The models proposed gather simplicity of formulation and easy calibration. These constitutive relations have been calibrated and used to define the behaviour of two commercial **AA**, namely **AA 5083-H116** and **AA 7075** frequently used in marine and aeronautical applications. The analytical predictions of the models are compared with those obtained from constitutive relations for **AA** reported in the literature (*a modified Johnson–Cook model and a phenomenological model*). From the analysis conducted the following conclusions can be reached:**AA**AA
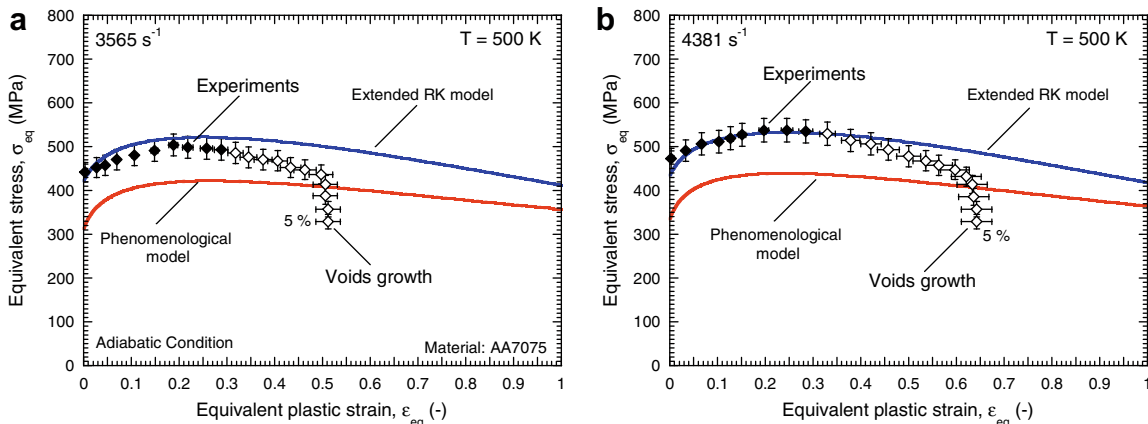

Fig. 19. Description of the flow stress evolution along plastic deformation using extended **RK** and **PM** models and comparison with experiments at $T_o = 500$ K [34]. (a) 3565 s^{-1}, (b) 4381 s^{-1}.

- The predictions provided by the extended **RK** models get satisfactory agreement with the experimental data. Such agreement is better than that obtained using the other constitutive relations examined for the whole range of strain rates and initial temperatures considered.
- The introduction of a new stress component in the original formulation of the **RK** model is necessary to obtain an accurate definition of the **DSA** effect. Neglecting the **NSRS** of certain **AA** was a common practice in traditional constitutive modeling. However, such procedure may lead to considerable disagreement between analytical predictions and experimental data.
- The strain rate sensitivity of many **FCC** metals cannot be defined using only the reciprocity strain rate-temperature proposed by Arrhénius equation. At high strain rate those materials (*among others*) show a strong increase of the flow stress due to viscous drag. Such behaviour is defined by the addition of an athermal stress-component to the original formulation of the **RK** model. Such procedure allows for a correct definition not just of the strain rate sensitivity but also of the temperature sensitivity of the material.

Moreover, both **RK** extensions reported could be applied at the same time in order to model a potential **AA** having **NSRS** and viscous drag at high rate of deformation, Fig. 20.

Acknowledgements

Appendix A. Derivatives of the extended RK constitutive relations for implementation into FE code

The extended **RK** constitutive relations reported in the paper can be implemented into **FE** code using for example the fully implicit algorithm reported in [35]. In order to conduct such implementation is necessary to obtain the first derivatives of the model. Those derivatives corresponding to the extensions proposed in this paper are reported below:

- Extended RK model to negative strain rate sensitivity

$$\left.\frac{d\sigma_T(\dot{\bar{\varepsilon}}^\mathrm{p}, \bar{\varepsilon}^\mathrm{p}, T)}{d\dot{\bar{\varepsilon}}^\mathrm{p}}\right|_{\bar{\varepsilon}^\mathrm{p}, T} = \frac{\sigma_0^\mathrm{ns} \cdot \left(1 - \frac{D_3 \cdot T_\mathrm{m} \cdot \log\left(\frac{\dot{\bar{\varepsilon}}^\mathrm{p}}{\dot{\varepsilon}_\mathrm{max}}\right)}{T}\right)}{\dot{\bar{\varepsilon}}^\mathrm{p}}$$
$$- \frac{D_3 \cdot T_\mathrm{m} \cdot \sigma_0^\mathrm{ns} \cdot \log\left(\frac{\dot{\varepsilon}_\mathrm{trans}}{\dot{\varepsilon}}\right)}{\dot{\bar{\varepsilon}}^p \dot{T}} \quad \text{(A-1)}$$

$$\left.\frac{d\sigma_T(\dot{\bar{\varepsilon}}^\mathrm{p}, \bar{\varepsilon}^\mathrm{p}, T)}{dT}\right|_{\bar{\varepsilon}^\mathrm{p}, \dot{\bar{\varepsilon}}^\mathrm{p}} = \frac{D_3 \cdot \sigma_0^\mathrm{ns} \cdot T_\mathrm{m} \cdot \log\left(\frac{\dot{\bar{\varepsilon}}^\mathrm{p}}{\dot{\varepsilon}_\mathrm{max}}\right) \cdot \log\left(\frac{\dot{\varepsilon}_\mathrm{trans}}{\dot{\bar{\varepsilon}}^p}\right)}{T^2} \quad \text{(A-2)}$$

- Extended RK model to viscous-drag

$$\left.\frac{d\sigma_T(\dot{\bar{\varepsilon}}^\mathrm{p}, \bar{\varepsilon}^\mathrm{p}, T)}{d\dot{\bar{\varepsilon}}^\mathrm{p}}\right|_{\bar{\varepsilon}^\mathrm{p}, T} = \alpha \cdot \chi \cdot \exp(-\alpha \cdot \dot{\bar{\varepsilon}}) \quad \text{(A-3)}$$

The derivatives corresponding to the original formulation of the **RK** model are reported in Rusinek et al. [44].

References

[1] Clausen AH, Børvik T, Hopperstad OS, Benallal A. Flow and fracture characteristics of aluminium alloy AA5083-H116 as function of strain rate, temperature and triaxiality. Mater Sci Eng A 2004;364:260–72.
[2] http://www.onera.fr/dmsc/modelisation-structures-composites.php.
[3] http://desourcesure.com/dss/2007/02/oiseaux_de_fer_contre_oiseaux.php.
[4] Rusinek A, Rodríguez-Martínez JA, Zaera R, Klepaczko JR, Arias A, Sauvelet C. Experimental and numerical analysis of failure process of mild steel sheets subjected to perpendicular impact by hemispherical projectiles. Int J Impact Eng 2009;36(4):565–87.
[5] Higashi K, Mukai T, Kaizu K, Tsuchida S, Tanimura S. Strain rate dependence on mechanical properties is some commercial aluminium alloys. J Phys III 1991.
[6] Mukai T, Higashi K, Tanimura S. Influence of the magnesium concentration on the relationship between fracture mechanism and strain rate in high purity Al–Mg alloys. Mater Sci Eng A 1994;76:181–9.
[7] Dorward RC, Hasse KR. Strain rate effects on tensile deformation of 2024-O and 7075-O aluminium alloy sheet. J Mater Eng Perform 1995;4:216–20.
[8] Cottrell AH. A note on the Portevin-Le Chatelier effect. Phil Mag (seventh series) 1953;44(335):829–32.
[9] Cottrell AH. Dislocations and plastic flow in crystals. Oxford: University Press; 1953.
[10] Sleeswijk AW. Slow strain hardening of ingot iron. Acta Metall 1958;6:598–603.
[11] Kubin LP, Estrin Y. Portevin-Le Chatelier effect in deformation with constant stress rate. Acta Metall 1985;33(3):397–407.
[12] Picu RC. A mechanism for the negative strain-rate sensitivity of dilute solid solutions. Acta Mater 2004;52:3447–58.
[13] Abbadi M, Hahner P, Zeghloul A. On the characteristics of Portevin-Le Chatelier bands in aluminum alloy 5182 under stress-controlled and strain-controlled tensile testing. Mater Sci Eng A 2002;337:194–201.
[14] Klose FB, Ziegenbein A, Hagemann F, Neuhäuser H, Hähner P, Abbadi M, et al. Analysis of Portevin-Le Chatelier serrations of type Bin Al–Mg. Mater Sci Eng A 2004;369:76–81.
[15] Zhang H, Ramesha KT, Chin ESC. High strain rate response of aluminum 6092/B4C composites. Mater Sci Eng A 2004;384:26–34.
[16] Brechet Y, Estrin Y. On the influence of precipitation on the Portevin-Le Chatelier effect. Acta Metall Mater 1995;43(3):955–63.
[17] Hähner P. On the critical conditions of the Portevin-Le Châtelier effect. Acta Mater 1997;45(9):3695–707.
[18] Zhang S, McCormick PG, Estrin Y. The morphology of Portevin-Le chatelier bands: Finite element simulation for Al–Mg–Si. Acta Mater 2001;49: 1087–94.
[19] McCormick PG. The Portevin-Le Châtelier effect in an Al–Mg–Si alloy. Acta Metall 1971;19:463–71.
[20] Follansbee PS. High-strain-rate deformation of FCC metals and alloys. Metallurgical applications of shock-wave and high-strain-rate phenomena; 1986. p. 451–79.
[21] Zerilli FJ, Armstrong RW. The effect of dislocation drag on the stress–strain behavior of fcc metals. Acta Metall Mater 1992;40:1803–8.
[22] Kapoor R, Nemat-Nasser S. Comparison between high strain-rate and low strain-rate deformation of tantalum. Metall Mater Trans 1999;31A:815–23.
[23] Nemat-Nasser S, Guo WG. Thermomechanical response of DH-36 structural steel over a wide range of strain rates and temperatures. Mech Mater 2003;35:1023–47.
[24] Kumar A, Hauser FE, Dorn JE. Viscous drag on dislocations in aluminum at high strain rates. Acta Metall 1968;9(16):1189–97.
[25] Campbell JD, Ferguson WG. The temperature and strain-rate dependence of the shear strength of mild steel. Phil Mag 1970;81:63–82.
[26] Regazzoni G, Kocks UF, Follansbee PS. Dislocation kinetics at high strain rates. Acta Metall 1987;12(35):2865–75.
[27] Perzyna P. Application of the thermodynamical theory of elasto-viscoplasticity in modern manufacturing processes. Course notes: Damage mechanics and micromechanics of localized fracture phenomena in inelastic solids. CISM. Udine, July 7-11, 2008.
[28] Zerilli FJ, Armstrong RW. Dislocation-mechanics-based constitutive relations for material dynamics calculations. J Appl Phys 1987;61:1816–25.
[29] Johnson GR, Cook WH. A constitutive model and data for metals subjected to large strains, high strain rates and high temperatures. In: Proceedings of seventh international symposium on ballistics; 1983. p. 541–7.
[30] Karagiozova D, Jones N. Dynamic buckling of elastic-plastic square tubes under axial impact II: structural response. Int J Impact Eng 2004;30:167–92.
[31] Børvik T, Forrestal MJ, Hopperstad OS, Warren TL, Langseth M. Perforation of AA5083-H116 aluminium plates with conical-nose steel projectiles – calculations. Int J Impact Eng 2009;36(3):426–37.
[32] Varas D, Zaera R, Lopez-Puente J. Numerical modelling of the hydrodynamic ram phenomenon. Int J Impact Eng 2009;36:363–74.
[33] Rusinek A, Klepaczko JR. Shear testing of sheet steel at wide range of strain rates and a constitutive relation with strain-rate and temperature dependence of the flow stress. Int J Plasticity 2001;17:87–115.
[34] El-Magd EM, Abouridouane M. Characterization, modelling and simulation of deformation and fracture behaviour of the light-weight wrought alloys under high strain rate loading. Int J Impact Eng 2006;32:741–58.

[35] Zaera R, Fernández-Sáez J. An implicit consistent algorithm for the integration of thermoviscoplastic constitutive equations in adiabatic conditions and finite deformations. Int J Solids Struct 2006;43:1594–612.

[36] Seeger A. The mechanism of glide and work-hardening in face-centered cubic and hexagonal close-packed metal. In: Dislocations and mechanical properties of crystals. New York: J. Wiley; 1957.

[37] Klepaczko JR. Thermally activated flow and strain rate history effects for some polycrystalline FCC metals. Mater Sci Eng 1975;18:121–35.

[38] Klepaczko JR. A general approach to rate sensitivity and constitutive modeling of FCC and BCC metals. In: Impact: effects of fast transient loadings, Rotterdam; 1998. p. 3–35.

[39] Rusinek A, Rodríguez-Martínez JA, Klepaczko JR, Pecherski RB. Analysis of thermo-visco-plastic behaviour of six high strength steels. J Mater Design 2009;30:1748–61.

[40] Klepaczko JR. A practical stress–strain–strain rate-temperature constitutive relation of the power form. J Mech Work Technol 1987;15:143–65.

[41] Nemat-Nasser S, Ni L, Okinaka T. A constitutive model for fcc crystals with application to polycrystalline OFHC copper. Mech Mater 1998;30:325–41.

[42] Oussouaddi O, Klepaczko JR. An analysis of transition from isothermal to adiabatic deformation in the case of a tube under torsion. Proceedings of the conference on DYMAT 91. J Phys IV 1991;Coll. C3(Suppl. III):C3–C323 [in French].

[43] Berbenni S, Favier V, Lemoine X, Berveiller N. Micromechanical modelling of the elastic–viscoplastic behaviour of polycrystalline steels having different microstructures. Mater Sci Eng 2004;372:128–36.

[44] Rusinek A, Zaera R, Klepaczko JR. Constitutive relations in 3-D for a wide range of strain rates and temperatures – application to mild steels. Int J Solids Struct 2007;44:5611–34.

[45] Klepaczko JR, Rusinek A, Rodríguez-Martínez JA, Pecherski RB, Arias A. Modeling of thermo-viscoplastic behaviour of DH-36 and Weldox 460-E structural steels at wide ranges of strain rates and temperatures, comparison of constitutive relations for impact problems. Mech Mater 2009;41:599–621.

[46] http://www.suppliersonline.com/propertypages/5086.asp.

[47] Benallal A, Berstad T, Børvik T, Hopperstad OS, Koutiri I, Nogueira de Codes R. An experimental and numerical investigation of the behaviour of AA5083 aluminium alloy in presence of the Portevin-Le Chatelier effect. Int J Plasticity 2008;24:1916–45.

[48] Rusinek A, Zaera R, Klepaczko JR, Cheriguene R. Analysis of inertia and scale effects on dynamic neck formation during tension of sheet steel. Acta Mater 2005;53:5387–400.

[49] Follansbee PS, Weertman J. On the question of low stress at high strain rates controlled by dislocation viscous. Iow Mech Mater 1982;1:345–50.

[50] Chiem CY. Material deformation at high strain rates. In: Meyers M, Murr L, Staudhammer K, editors. Shock-wave and high-strain-rate phenomena in materials. New York: Marcel Dekker; 1992. p. 69–85.

[51] Nemat-Nasser S, Guo WG, Kihl DP. Thermomechanical response of AL-6XN stainless steel over a wide range of strain rates and temperatures. J Mech Phys Solids 2001;49:1823–46.

[52] Guo WG, Nemat-Nasser S. Flow stress of Nitronic-50 stainless steel over a wide range of strain rates and temperatures. Mech Mater 2006;38:1090–103.

[53] http://www.alcoa.com/mill_products/catalog/pdf/alloy7075techsheet.pdf.

[54] El-Magd E. Mechanical properties at high strain rates. J Phys IV 1994;C8(4):149–70.